Spectroscopy of atomic orbital sizes using bi-elliptical high-order harmonic generation

Eliyahu Bordo,[1,*] Ofer Neufeld,[1,*] Ofer Kfir,[2] Avner Fleischer,[3] and Oren Cohen[1]

[1]*Solid State Institute and Physics Department, Technion–Israel Institute of Technology, Haifa 3200003, Israel*

[2]*4th Physical Institute, University of Göttingen, Göttingen 37077, Germany*

[3]*Raymond and Beverly Sackler Faculty of Exact Science, School of Chemistry and Center for Light-Matter Interaction, Tel Aviv University, Tel-Aviv 6997801, Israel*

(Received 20 May 2019; published 25 October 2019)

We report that high-order harmonic generation (HHG) of atoms driven by ω-2ω bi-elliptical pumps exhibits a substantial sensitivity to variation of the spatial extent of the participating valence orbitals and effective potential. We identify the physical mechanisms responsible for this enhanced sensitivity through theoretical investigations in atomic He, Ne, Ar, and Kr systems using several quantum models. We demonstrate this size sensitivity experimentally by measuring significant disparities in the bi-elliptical HHG spectra of atomic Ar and Kr, which have relatively similar ionization potentials, but substantially different p-shell sizes and effective potentials. This result may be useful for ultrafast spectroscopy which is sensitive to effective potentials and orbitals.

DOI: 10.1103/PhysRevA.100.043419

I. INTRODUCTION

High-order harmonic generation (HHG) is a nonlinear process that occurs when gas, liquid, or solid media are irradiated by an intense laser field [1–4]. The light-matter interaction upconverts the pump laser's frequency, generating a spectrally broad coherent source of high-order harmonics with photon energies reaching as high as the keV range [1,2,4]. This unique process has been investigated for several decades, and utilized in numerous applications, including high-resolution imaging and ultrafast science [1,2,4,5]. In particular, HHG provides an exceptional and often irreplaceable spectroscopic tool, as it allows probing dynamical processes on the atomic or molecular level in their natural timescales (down to attoseconds). This sensitivity may be utilized either by downstream experiments using attosecond pulses that are generated by HHG, or alternatively, through so-called HHG spectroscopy, which extracts information about the medium and strong-field processes by analyzing the harmonic spectra themselves. For instance, HHG spectroscopy was utilized to probe tunnel ionization dynamics [6,7], molecular alignment [8,9], multielectron dynamics [10–12], molecular [13,14] and atomic [15] orbitals, topological properties of condensed matter [16,17], and more.

Recently, high-order harmonic spectroscopy using bicircular and bi-elliptical pumps (i.e., where the HHG driving pulse comprises two copropagating beams with counterrotating circular or elliptical polarizations) has been employed for several applications, including investigating conservation of spin angular momentum [18–21], orbital angular momentum [22], symmetry breaking [23], symmetry properties of molecules and solids [24,25], and chirality [26–32].

Here we utilize bi-elliptical HHG spectroscopy to theoretically and experimentally explore the spatial extent of orbitals and the effective potential in noble gases. These properties can be probed with ultrafast time resolution using orbital-tomography techniques [13,33,34], though our presented bi-elliptical approach may exhibit some advantages including not relying on reconstruction algorithms and semiclassical assumptions. Our calculations show that HHG in the bi-elliptical configuration is highly sensitive to the atomic potential well and to the size of its valence orbitals, even for systems with similar ionization potential and valence shell configurations. This phenomenon is accentuated when the harmonic response is measured over the full range of pump ellipticities. We theoretically analyze the effect and classify the responsible physical mechanisms. The orbital size dependence is observed experimentally as disparities in the bi-elliptical intensity-resolved spectrograms (henceforth referred to as "spectrograms") from Ar and Kr noble gases.

II. THEORATICAL ANALYSIS

We start by theoretically exploring HHG from noble gas media driven by a bi-chromatic laser in a bi-elliptical configuration. We will numerically demonstrate that the spectrograms provide sensitivity to the atomic species, and in particular, to the spatial extent of the effective atomic potential well and its valence states.

We first consider the following bi-chromatic (ω-2ω), bi-elliptical, pump field:

$$\vec{E}(t) = \frac{A(t)E_0}{\sqrt{1+\varepsilon^2}}\mathrm{Re}\left\{e^{i\omega t}(\hat{x}+i\varepsilon\hat{y}) + \Delta e^{2i\omega t+\phi}(\hat{y}-i\varepsilon\hat{x})\right\}, \tag{1}$$

where E_0 is the field amplitude, ε is the ellipticity of both the ω and 2ω beams, Δ and ϕ are the amplitude ratio and relative phase between the beams, respectively; the spatial dependence of the beams has been neglected in the dipole approximation; and $A(t)$ is the following dimensionless supersine envelope

[*]These authors contributed equally to this work.

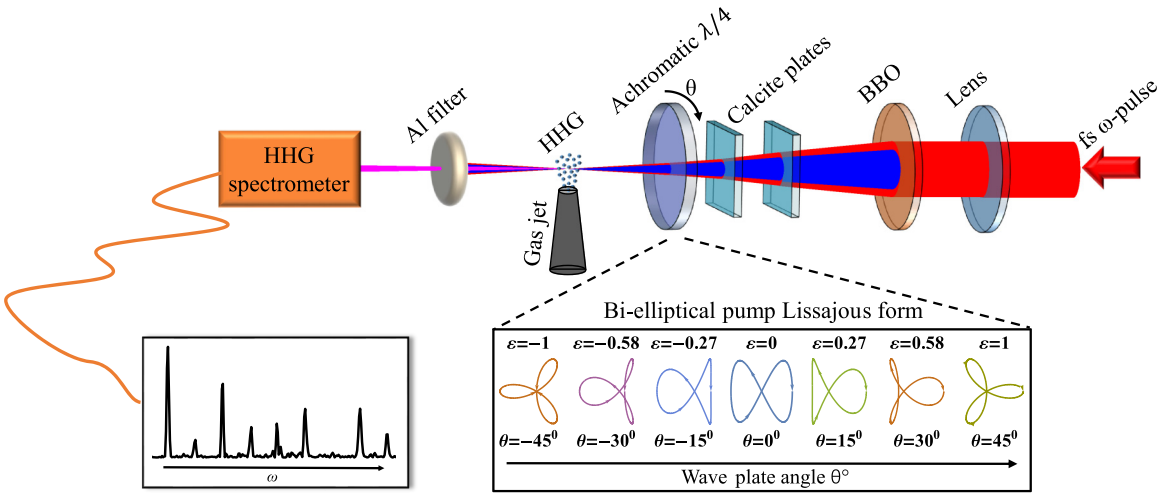

FIG. 1. Bi-elliptical (ω-2ω) HHG scheme illustration and in-line experimental setup through the MAZEL-TOV apparatus [21]. A linearly polarized femtosecond pulse of frequency ω (indicated by the red beam) is partially frequency up-converted by second-harmonic generation in a BBO crystal (indicated by the blue beam). The ellipticities of both beams are simultaneously controlled all the way from -1 to 1 using a rotatable achromatic quarter-wave plate. The resulting bi-chromatic pump fields for different values of ε are shown schematically in the 2D Lissajous plots for the field polarization in the xy plane (schematically drawn for $\Delta = 1$, $\phi = \pi/2$), where arrows indicate the direction of time. The harmonic spectrum is then measured as a function of ε using an XUV spectrometer to produce the spectrograms. For further experimental details, see Appendix C.

function [35]:

$$A(t) = \left\{ \sin\left(\frac{\pi t}{NT}\right) \right\}^{\frac{\pi}{\sigma}\left|\frac{t}{NT}-\frac{1}{2}\right|}, \quad 0 \leqslant t \leqslant NT, \tag{2}$$

where N is the number of optical cycles in the pulse, $T = 2\pi/\omega$ is the optical period, and we set $\sigma = 0.4$ which leads to a full width at half maximum (FWHM) of $0.4NT$ in the pulse intensity (this envelope function is similar to the often used super-Gaussian envelope with a tunable FWHM, but conveniently upholds $A(t = 0) = A(t = NT) = 0$; hence it poses some numerical advantages).

The field in Eq. (1) describes copropagating ω and 2ω beams that are both elliptically polarized with an ellipticity ε, but have an opposite handedness and orthogonal major elliptical axes. This pump field has several independent degrees of freedom (DOF), including absolute intensity, relative phases, amplitude ratios, etc.; importantly, the ellipticity DOF, ε, is fully controlled from -1 to 1, yielding HHG traces (spectrograms) with respect to ε (see Fig. 1 for scheme illustration and setup).

Next, we describe the interaction of the above laser field with gas media, resulting in HHG. We use a 2D quantum-mechanical model for an atom interacting with the bi-chromatic laser field, where the atomic gas is described microscopically by a single-electron Hamiltonian, given in atomic units by

$$H_0 = -\frac{1}{2}\nabla^2 - \frac{1 + Ze^{-\beta r^2}}{\sqrt{r^2 + \alpha}}, \tag{3}$$

where the left term in H_0 is the electron's kinetic energy, and the right term represents a spherically symmetric softened Coulomb effective potential (EP) with screening. The screening parameter Z is chosen according to the number of valence electrons in the atomic species, where we set $Z = 7$ for the noble gases Ne, Ar, and Kr (assuming deeper core levels are irrelevant). β defines the effective screening length and is related to the atomic core-shell size. Previous studies set $\beta = 1$ for convenience [36–38]. The softening parameter α is used to smoothen the Coulomb well, and is usually freely adjusted in order to get an ionization potential (I_p) that corresponds to the experimental value of the atomic species [36–43]. Here we follow a different approach, and adjust α and β simultaneously to arrive at the desired I_p, but also control the physical size of the valence orbitals. This approach generates a family of EPs that differ in the size of their valence states, but not in their I_p. We now explicitly focus on two separate EP models of atomic Ne gas. For model 1 we set $\alpha_1 = 0.27, \beta_1 = 3.12$, and for model 2, $\alpha_2 = 3.70, \beta_2 = 0.55$. These two EPs have identical ionization potentials from the $2p$ levels that describe atomic Ne ($I_p = 0.79$ hartree), but result in orbitals that differ in size by $\sim$20% (see Fig. 2).

The interaction of these species with the laser field is described within the dipole approximation and in the length gauge through the full Hamiltonian,

$$H(t) = H_0 + \vec{E}(t) \cdot \vec{r}, \tag{4}$$

with which the time-dependent Schrödinger equation (TDSE) can be solved independently for each of the valence states. Since noble gases with degenerate valence p shells are considered, it is assumed that the atom is in a pure state of electrons occupying p orbitals pointing in an arbitrary direction in space. In order to describe the coherent emission from this atomic ensemble, we perform orientation averaging. The orientation averaging is equivalent to performing just two representative calculations—one starting from the p_+ orbital, and the other from the p_- orbital, where the harmonic emission from these two orbitals is summed (see Appendix A for details).

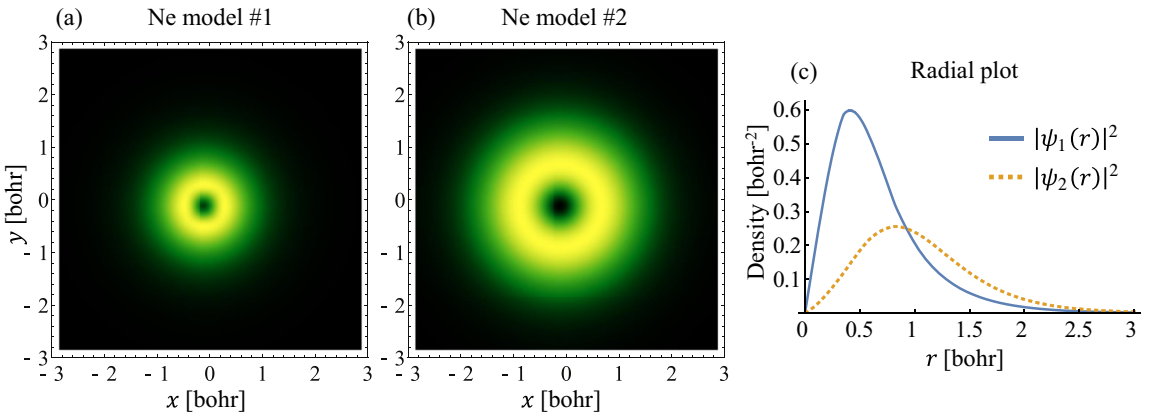

FIG. 2. Two effective potential models for atomic Ne gas. (a) Model 1: probability density in valence $2p$ state from Eq. (3) with $\alpha_1 = 0.27$, $\beta_1 = 3.12$ resulting in valence states ∼3.4 bohrs wide. (b) Model 2: probability density in valence $2p$ state from Eq. (3) with $\alpha_2 = 3.70$, $\beta_2 = 0.55$ resulting in valence states ∼4.1 bohrs wide. (c) Radial probability density and potential plots comparing models 1 and 2. The examined models have p-orbital spatial extents that differ by 20%, but the same $I_p = 0.79$ hartree (experimental value Ne).

Figures 3(a) and 3(b) present the spectrograms from these two models—the calculated HHG spectral intensity as a function of $-1 \leqslant \varepsilon \leqslant 1$. Before addressing the differences between the spectrograms, we first analyze their common structure, as investigated in Ref. [21]. The intensity measurements span two separate regimes in bi-elliptical HHG: (I) for $\varepsilon = \pm 1$ the pump beam is bi-circular and exhibits a threefold rotational dynamical symmetry (DS) [19,44,45] (see Fig. 1). In this regime, only circularly polarized $3n \pm 1$ harmonics are emitted for integer n [see suppression of $3n$ harmonic intensity in Figs. 3(a) and 3(b)], and there are three identical recollision events per optical cycle separated by $\Delta t = T/3$, and angles 120° [43,46]. (II) On the other hand, for $\varepsilon = 0$ the pump beams are cross-linearly polarized and maintain a reflection DS along the y axis [43] (see Fig. 1). In this regime, the harmonic emission in all orders is symmetry allowed, but mostly odd harmonics are emitted because the ω beam is more intense than the 2ω beam (Fig. 3 is calculated for $\Delta = 1/\sqrt{5}$). We further note that for $\varepsilon = 0$ there are two identical (but nonparallel) recollision events per optical cycle, separated by $\Delta t = T/2$, [47,48]. By tuning ε away from these specific values, the DS in each regime is broken, which manifests in the HHG process as variations in the recollision events occurring within each optical cycle, that now become separated by an additional time delay, $\Delta t + \delta t(\varepsilon)$ [21], where $\delta t(\varepsilon)$ represents the time delay between subsequent recollision events. The delay $\delta t(\varepsilon)$ varies with ε; hence, the temporal interference of the recollision events results in pronounced intensity oscillations per harmonic order in the spectrograms (see Fig. 3). In addition, for $-0.5 < \varepsilon < 0.5$ the spectrum oscillates between the dominance of odd- or even-harmonic orders [see dashed white lines in Fig. 3(a)]. Another noticeable feature is that the harmonic yield is symmetric about $\varepsilon = 0$. Importantly, the intensity oscillations along the ε axis can

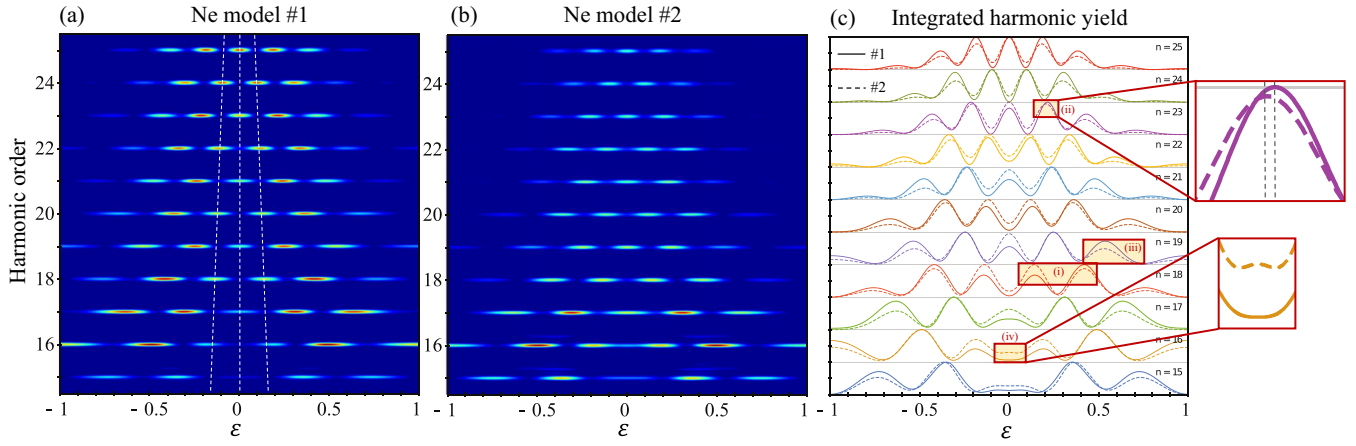

FIG. 3. Numerical results: bi-elliptical (ω-2ω) HHG spectrograms from two separate models for atomic Ne (see Fig. 2) with $I_0 = 3 \times 10^{14}$ W/cm^2, $\Delta = 1/\sqrt{5}$, $\phi = \pi/2$, $N = 28$, $\lambda = 800$ nm. (a) Spectrogram from atomic Ne model 1. (b) Same as (a) but for atomic Ne model 2. The intensity in the spectrogram is plotted in a linear scale. (c) Integrated harmonic intensity per harmonic as a function of ε for both models of Ne; solid line for model 1 and dashed line for model 2. In (c) the intensity of each harmonic is normalized to the maximal intensity along the ε axis for clarity. The figure shows distinct differences in the spectrograms from the two models. Differences pointed out in the text are highlighted by a red box and insets with their associated index.

provide spectroscopic sensitivity to the target species, either in the relative amplitudes of the peaks, or in the structure of each peak.

We now focus on the differences between the spectrograms. Figures 3(a) and 3(b) differ in the relative peak structures of each harmonic. For brevity, we focus on four distinct features [as indicated by red boxes and associated indices in Fig. 3(c)]: (i) In model 1 the peak centered around $\varepsilon \approx 0.15$ in harmonic 18 is smaller than the peak centered around $\varepsilon \approx 0.45$, while the opposite is correct in model 2; (ii) harmonic 23 is maximized at $\varepsilon \approx 0.21$ for model 1, while it is maximized at $\varepsilon \approx 0.19$ for model 2; (iii) the peak centered around $\varepsilon \approx 0.54$ at harmonic 19 is wider in model 1 than in model 2; i.e., the peak is broadened in the ε domain; and (iv) harmonic 16 shows a peak at $\varepsilon = 0$ from model 2 that is missing in model 1. While each harmonic spectrum per ε by itself does not differ substantially between the models, we find that the full spectrogram shows sensitivity to the atomic species. The sensitivity stems from the large amount of information captured by the spectrogram, which spans a large bandwidth and several HHG regimes.

Notably, the Appendix F section presents similar calculations for two other standard methods of HHG spectroscopy: ω-2ω bi-chromatic pumps where the relative phase between the pumps is scanned [6,7], and a monochromatic elliptical pump where the ellipticity is scanned [49]. In both cases, the spectrograms are less sensitive to the atomic species and orbital spatial extents. We attribute the enhanced sensitivity of our proposed scheme to the fact that the bi-elliptical scanning covers significantly different regimes in the HHG process, e.g., transition from two to three recollision events per optical cycle. Therefore, bi-elliptical spectrograms offer enhanced sensitivity to the orbital sizes, and possibly also other spectroscopic advantages.

It is instructive to discuss the physical mechanisms that lead to the observed sensitivity. Notably, this quantum-mechanical effect is not described by the semiclassical three-step model which neglects the long-range Coulomb potential and the spatial extent of the participating electronic states [50]. The effect originates from several interrelated mechanisms, each corresponding to a physical effect that is typically ignored in one of the steps of the three-step model:

(1) The ionization step is sensitive to the valence orbital size and shape. Wider orbitals are usually associated with larger polarizabilities and ionize more easily [10,51,52], which can lead to variations in the harmonic yield in both spectrograms.

(2) The motion of the electronic wave packet in the continuum is sensitive to the structure of the potential well. This can be intuitively interpreted as Coulomb corrections to the electron's trajectory [53,54]—while both models have a long-range columbic dependence, their Coulomb softening parameters slightly differ. This results in different time delays between recollisions, to which a relative time shift can be assigned-$\delta(\delta t(\varepsilon))$. Even small delays can lead to large phase shifts for high-order harmonics [$\delta\phi = n\omega\delta(\delta t(\varepsilon))$ is linearly proportional to the harmonic order, n]. This effect leads to variations in the peak centers between the models as observed throughout the spectrogram, because the peak maxima (and minima) are found for a specific value of $\delta t(\varepsilon)$ which maximizes (minimizes) the response.

(3) The final step of HHG, the recombination, is sensitive to the valence orbital. This originates from the orbital dependence of the recombination matrix elements between the ionized electron wave packet and the atomic ground state [4]. For example, wider states allow for a larger impact parameter for the recolliding electron, meaning that larger ellipticities still result in harmonic emission. This effect thus broadens or narrows the peaks along the ε axis in the spectrogram, and also changes their intensities.

These three mechanisms are intertwined and difficult to separate. In practice, they all play a role in the dynamics, as peak broadening, shifting, and intensity variations are all evident in the spectrograms. Appendix D presents calculations for atomic He (valence s shell) that show similar results, demonstrating the generality of our analysis.

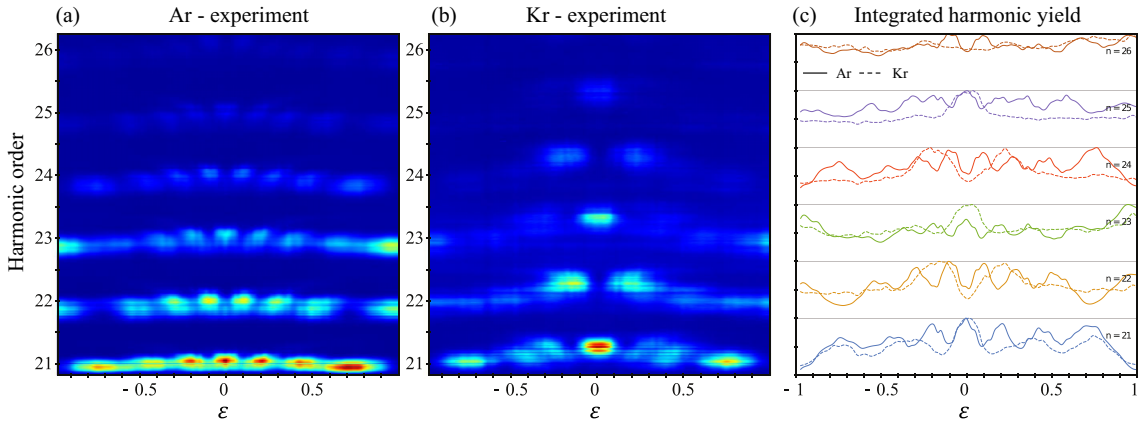

FIG. 4. Experimental results: bi-elliptical (ω-2ω) HHG spectrograms from atomic Ar and Kr gases with $I_0 \sim 3 \times 10^{14}$ W/cm^2, $\Delta = 1/\sqrt{3}$, $N \sim 11$, $\lambda = 790$ nm. (a) Spectrogram from atomic Ar, and (b), from atomic Kr. The intensity in the spectrogram is plotted in a linear scale. (c) Integrated harmonic intensity dependence on ε from both media. In (c) the intensity of each harmonic is normalized to the maximal intensity along the ε axis for clarity. The figure shows distinct differences in the spectrograms from these noble gases, even though they have relatively similar ionization potentials and valence shell structure. The frequency of the HHG slightly depends on the ellipticity since the two field components have a spectral mismatch (the 2ω field is not exactly twice the frequency of the ω field).

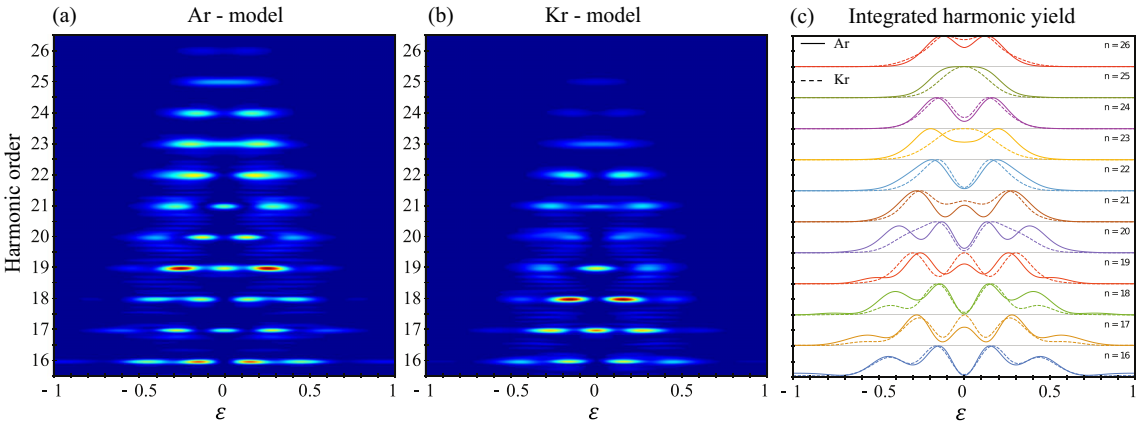

FIG. 5. Numerical results: bi-elliptical (ω-2ω) HHG spectrograms from atomic Ar and Kr models with $I_0 = 10^{14}\,\mathrm{W/cm^2}$, $\Delta = 1/\sqrt{5}$, $\phi = \pi/2$, $N = 24$, $\lambda = 800\,\mathrm{nm}$. (a)–(c) Same as in Fig. 4 but from numerical calculations for 2D effective potential models that have the correct I_p for each species, and also the p-shell spatial extents that match ground-state DFT calculations.

It is worth comparing the results obtained from the exact integration of the TDSE to strong-field approximation (SFA) calculations (with an approach similar to that in Ref. [20]; see Appendix E). In SFA calculations, the spatial extent of the orbital enters through the transition dipole matrix elements, while Coulomb corrections are neglected [55]. We find that the SFA calculations show much weaker dependence on the orbital sizes than in the TDSE approach. Notably, the effect of peak maxima (or minima) shifting along the ε axis that is observed within the TDSE calculations (due to different-sized orbitals), is absent within the SFA approach. This numerically supports our suggested mechanism for this phenomenon—Coulomb corrections to the electron trajectory in the continuum.

III. EXPERIMENTAL RESULTS

To demonstrate the orbital-size sensitivity of bi-elliptical HHG, we measure the harmonic emission as a function of the bi-elliptical pump ellipticities in atomic Ar and Kr. These noble species have similar ionization potentials of 0.58 and 0.51 hartree, respectively ($\Delta I_p = 1.15\omega$ where ω corresponds to a photon at 800 nm). Both gases also share a p-shell valence structure, but differ in the spatial extent of their valence orbital and binding-potential structure. Consequently, Ar and Kr are ideal candidates to test the effect of the orbital-size sensitivity on HHG.

The experimental setup is described in Fig. 1 and realized using a fully in-line MAZEL-TOV apparatus as described in Ref. [21] (see Appendix C). Figure 4 presents the spectrograms from these two species, showing several clear disparities. The most dominant difference is that intensities of harmonic peaks along ε are relatively constant throughout the spectrogram in Ar, while they are much stronger near $\varepsilon = 0$ in Kr, which persists in all harmonic orders. To discern whether this disparity indeed results from sensitivity to the atomic well and its valence states, the spectrograms should be analyzed in comparison to theory.

For this purpose, we construct a quantum-mechanical model for Ar and Kr in the spirit of the model presented in Sec. II for Ne. We choose α and β parameters for the EP in Eq. (3) that reproduce the experimental I_p values in the p shells of both gases, but also result in p orbitals that correspond to the *ab initio* calculated spatial extents of the three-dimensional (3D) p shells from density functional theory (DFT) (see Appendix B). This approach generates an EP model for Ar with the parameters $\alpha_{\mathrm{Ar}} = 0.995$, $\beta_{\mathrm{Ar}} = 1.760$, leading to a p shell that is 4.3 bohrs wide, and an EP model for Kr with the parameters $\alpha_{\mathrm{Kr}} = 4.290$, $\beta_{\mathrm{Kr}} = 0.700$, leading to a p shell that is 4.9 bohrs wide (the relative difference is $\sim$14%). The corresponding numerical results are presented in Fig. 5, and show trends that are similar to those observed experimentally, where Kr favors stronger peaks around $\varepsilon = 0$ compared to Ar (note that calculations are performed for a weaker laser power to avoid ground-state depletion). These results support our conclusion that the measured effects are caused by the sensitivity of the bi-elliptical HHG scheme to the valence orbital and the effective potential structure of the noble gas.

Lastly, we refer the reader's attention to an interesting observed experimental feature—the measured spectrogram of Ar contains one additional intensity oscillation along the ε axis compared to the spectrogram from Kr [see Fig. 4(a) around $\varepsilon \approx 0.3$]. Our theoretical calculations do not reproduce this feature for any model parameters. We hypothesize that it is caused by either propagation effects, or multielectron effects (both neglected in our model), which should be explored in future work.

IV. CONCLUSIONS

In this paper we theoretically and experimentally demonstrated that scanning the ellipticity of bi-elliptical pumps in HHG can be a sensitive knob for probing the spatial extents of valence orbitals and effective potential structures of atomic systems. This effect, which is neglected in the standard three-step model for HHG [50], and is not fully described by standard SFA calculations, becomes non-negligible in the full bi-elliptical intensity-resolved spectrograms that are measured as a function of pump ellipticities. We theoretically analyzed the effect using a direct quantum-mechanical model in atomic noble gases (He, Ne, Ar, and Kr), and classified the

responsible physical mechanisms. Experiments were carried out in atomic Ar and Kr gases (that have similar ionization potentials and p-shell structures), showing distinct disparities in the bi-elliptical HHG spectrograms from these species. By comparing the results to theoretical models, we showed that these discrepancies arise from the different p-shell sizes and effective potentials of these atoms, demonstrating the atomic species sensitivity of bi-elliptical HHG spectroscopy.

Our results could be used for ultrafast spectroscopy of various quantities, such as the magnitude of Coulomb corrections in strong-field processes, the intrinsic dipole phase of emitted harmonics [56], the shape and size of the atomic orbitals, and the effective potential structure of the ionized target. Another exciting prospect is the extension of the current theoretical model and technique to spectroscopically probe molecular orbitals of oriented or unoriented gas, as well as solid media. The bi-elliptical scheme can be especially appealing as it can be utilized to simultaneously probe several intrinsic parameters of the medium, as was shown for chirality [30]. Lastly, while we considered here the sensitivity of the bi-elliptical scheme in the HHG yield, a similar approach could be developed utilizing the sensitivity in the ellipticity of the emitted harmonics, which is expected to carry additional information on the ultrafast dynamics in the medium.

ACKNOWLEDGMENTS

This work was supported by the Israel Science Foundation (Grant No. 1781/18), and the Wolfson foundation. O.N. gratefully acknowledges the support of the Adams Fellowship Program of the Israel Academy of Sciences and Humanities. O.K. gratefully acknowledges funding from the European Union's Horizon 2020 research and innovation programme under the Marie Sklodowska-Curie Grant Agreement No. 752533.

APPENDIX A: NUMERICAL MODEL DETAILS

This Appendix describes the details of the numerical HHG calculations for the atomic species presented in the main text. We first describe how the eigenstates of the EP models in Eq. (3) in the main text were numerically found, and then how the TDSE was solved.

The Hamiltonian in Eq. (3) in the main text was repeatedly diagonalized (for a surface of α and β parameters) in order to generate the desired parameter choices that produce the experimental ionization potential values and allow control over the valence orbital spatial extents. This was accomplished by separation of variables for the two-dimensional (2D) time-independent Schrödinger equation into a radial equation and an azimuthal equation [57]. The azimuthal equation was analytically quantized with the quantum number $-l < m < l$, where l is the total angular momentum, and solved with the azimuthal eigenfunctions $e^{im\theta}$. The radial equation was solved numerically using the basis of 250 Bessel functions of the first kind [58], where the matrix elements integration was performed numerically on a radial grid spanning up to $L = 60$ bohrs with spacing $\Delta r = 0.0097$ bohr. The desired α and β parameters were extracted from these calculations. For the chosen α and β parameters, H_0 was also diagonalized using imaginary time evolution combined with a Gram-Schmidt algorithm (by solving the TDSE as next described) in order to obtain numerically exact eigenstates for H_0 represented on a Cartesian grid (which is used for the HHG calculations that are described next). The eigenstates up to the valence shell were found to a self-consistency tolerance of 10^{-13} hartree in energy, and 10^{-6} maximal wave function difference.

Next, the TDSE for the time-dependent Hamiltonian in Eq. (4) in the main text was solved numerically in the length gauge using a third-order split operator method [59,60]. The spatial grids were discretized on an $L \times L$ Cartesian grid for $L = 120$ bohrs with spacing $\Delta x = \Delta y = 0.2348$ bohr. The time grid was discretized using spacing $\Delta t = 0.025$ a.u. Convergence was tested with respect to the grid densities and sizes. In order to avoid reflections, absorbing boundaries were used with the absorber:

$$V_{ab}(\vec{r}) = -i\eta(|\vec{r}| - r_0)^{\alpha}\Theta(|\vec{r}| - r_0), \tag{A1}$$

where $\eta = 5 \times 10^{-4}$ a.u., $\alpha = 3$, Θ is a step function, and $r_0 = 36$ bohrs. The initial states were chosen as equally populated $2p$ states ($2p_+$ and $2p_-$) for Ne, Ar, and Kr, and a $1s$ state for He (each initial state is propagated separately under the one-electron Hamiltonian). This choice is convenient compared to choosing initially populated $2p_x$ and $2p_y$ states, because the laser-matter interaction needs to be orientation averaged. Consequently, when choosing $2p_x/2p_y$ initial states the harmonic response must be calculated for the full 2π azimuthal angles of the laser polarization axis with respect to the initial orbital axis, and averaged. However, the $2p_+/2p_-$ states are radially symmetric, rendering the HHG response from any azimuthal angle (between the laser field and the $2p_+/2p_-$ orbitals) identical. The orientation averaging is then carried out by coherently adding the response from the $2p_+$ and $2p_-$ states in a single oriented calculation. That is, the total dipole acceleration from all occupied states for p-type atoms is calculated as follows:

$$\vec{a}_{\rm tot}(t) = -\langle 2p_+(t)|\vec{\nabla}V + \vec{E}(t)|2p_+(t)\rangle - \langle 2p_-(t)|\vec{\nabla}V + \vec{E}(t)|2p_-(t)\rangle \tag{A2}$$

where $\vec{a}_{\rm tot}(t)$ is the total dipole acceleration, and where the notation $|2p_\pm(t)\rangle$ refers to the exact field-dressed orbital that is propagated under the full Hamiltonian and interacts with the laser pulse, i.e.:

$$|2p_\pm(t)\rangle = \exp\left\{-i\int_0^t dt' H(t')\right\}|2p_\pm(t=0)\rangle, \tag{A3}$$

and where we used the Ehrenfest theorem [61] in cases where the total amount of electronic density absorbed did not exceed 7% (for Ne and He models that have relatively large I_p). In case the total amount of electronic density absorbed exceeded 7% (in Ar and Kr models that have relatively low I_p), the induced dipole was calculated directly through

$$\vec{r}_{\rm tot}(t) = -\langle 2p_+(t)|\vec{r}|2p_+(t)\rangle - \langle 2p_-(t)|\vec{r}|2p_-(t)\rangle, \tag{A4}$$

from which the dipole acceleration was calculated by a second-order derivative using a fifth-order finite difference approximation. From Eqs. (A2) and (A4) the harmonic spectra were calculated by Fourier transforms. In the case of atomic He, the valence state is s type and nondegenerate, so the

total harmonic response is calculated directly from the single-electron response.

APPENDIX B: DFT CALCULATION DETAILS

In order to choose the most appropriate EP model for atomic Ar and Kr, we performed 3D *ab initio* calculations to extract the physical size of the noble gases' p shells. We performed density functional theory (DFT) calculations using the real-space OCTOPUS code [62–64], within non-polarized DFT (neglecting the spin DOF) within the local density approximation (LDA) [65]. The core [Ne] and [Ar] shells of Ar and Kr atoms, respectively, were represented using Hartwigsen-Goedecker-Hutter LDA norm-conserving pseudopotentials [66]. The real-space grid was discretized on a spherical grid of radius 15 bohrs, and spacing $\Delta x = \Delta y = \Delta z = 0.15$ bohr, and the Kohn-Sham equations were solved to self-consistency $< 5 \times 10^{-7}$ hartree. The p-shell size was extracted from the p_+/p_- states according to the radial distance from which the probability density reduces below 10^{-3} compared to the maximal density in the orbital (the same criterion is used to evaluate the orbital sizes in 2D calculations).

APPENDIX C: EXPERIMENTAL DETAILS

The experimental setup for bi-chromatic (ω-2ω), bi-elliptical, HHG (schematically illustrated in Fig. 1 in the main text) followed the in-line MAZEL-TOV geometry used in Ref. [21], and consisted of a linearly polarized pulsed laser beam generated by a Ti:sapphire amplifier (1 kHz, $\lambda_0 = 790$ nm, FWHM = 27 fs, 1 mJ). The s-polarized fundamental pulse was partially up-converted into a second-harmonic (SH) beam with a perpendicular p-polarized field ($\lambda_{SH} = 395$ nm) using a beta-phase barium borate (BBO) crystal (0.2 mm, cutting angle 29.2° for type-I phase matching). The power in the fundamental and SH beams was measured to be 0.9 and 0.1 W, respectively ($\Delta = 1/\sqrt{3}$). The bi-chromatic beam was then passed through two calcite plates (55° cut with respect to the optical axis, 1 mm thick, AR coated) that compensate for the group delays induced along the optical path. The plates are inversely oriented in order to cancel shifts caused by Snell's law and birefringent walk-offs. The delay between the fundamental and SH pulses (caused by the calcite plates) was compensated for by the quarter-wave plate and the vacuum chamber entrance window such that the two beams temporally overlapped in the gas jet. The exact delay was tuned by rotating the calcite plates, and set to zero, to maximize the yield (the relative phase ϕ between the beams was not measured, and was chosen as $\phi = \pi/2$ in calculations). The bi-chromatic cross-linearly polarized beam was then passed through an achromatic quarter-wave plate, whose rotation angle (θ) directly controlled the ellipticity of both beams through the relation $\varepsilon = \tan(\theta)$. The bi-elliptical beam then entered the vacuum chamber of pressure 10^{-3}–10^{-2} torr (through a perpendicular 2-mm fused silica window) and was focused using the initial lens ($f = 500$ nm, focusing both beams to a joint focus) into the noble gas jet that was positioned in the chamber. The resulting HHG beam was separated from the pump beams using a thin aluminum foil (0.2 μm thick). The HHG spectrum was recorded with a spectrometer comprising a blazed grating, a toroidal mirror, and an XUV charge-coupled device (CCD). We measured the spectrum while rotating the quarter–wave plate at $\Delta\theta = 1°$, and the total acquisition time of the full spectrogram is 20 min.

APPENDIX D: RESULTS IN HELIUM

In this Appendix, we present numerical results complementary to those presented in the main text for atomic He that has valence s states. The EP for atomic He is chosen similar to Eq. (3) in the main text, but with $Z = 1$, and the two parameters α and β are accordingly adjusted to arrive at the experimental ionization potential of He ($I_p = 0.90$ hartree), but also control the spatial extent of the s shell. Figure 6 presents a comparison between two models that differ by 16% in the size of their s orbitals, showing results that are in the same spirit as those presented in the main text—the spectrogram are sensitive to the size of the s orbitals and the effective potential that generates them, via all of the identified mechanisms.

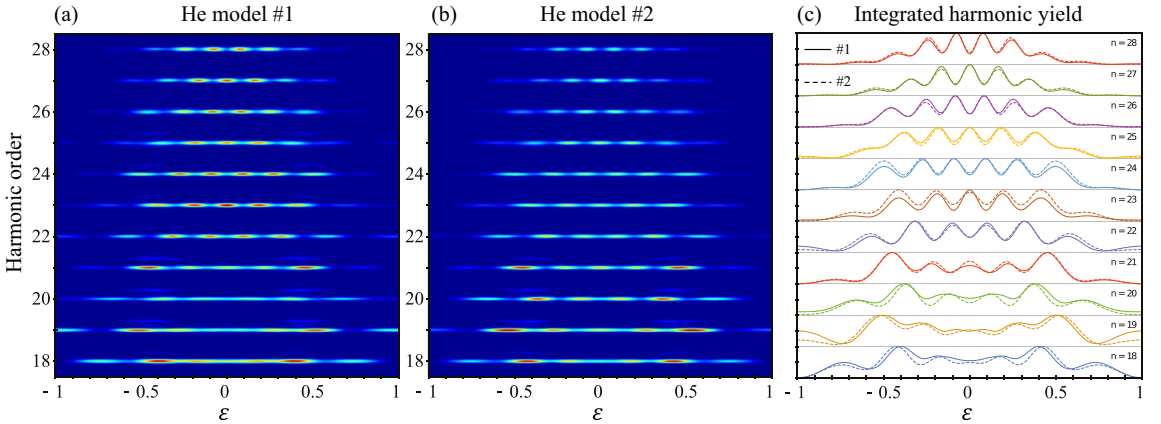

FIG. 6. Numerical results: bi-elliptical (ω-2ω) HHG spectrograms from atomic He models with $I_0 = 3 \times 10^{14}$ W/cm^2, $\Delta = 1/\sqrt{5}$, $\phi = \pi/2$, $N = 28$, $\lambda = 800$ nm. (a)–(c) Same as in Fig. 3 in the main text, but from effective potential models generated with the parameters $\alpha = 0.29, 1.09$, $\beta = 4.25, 0.22$, respectively.

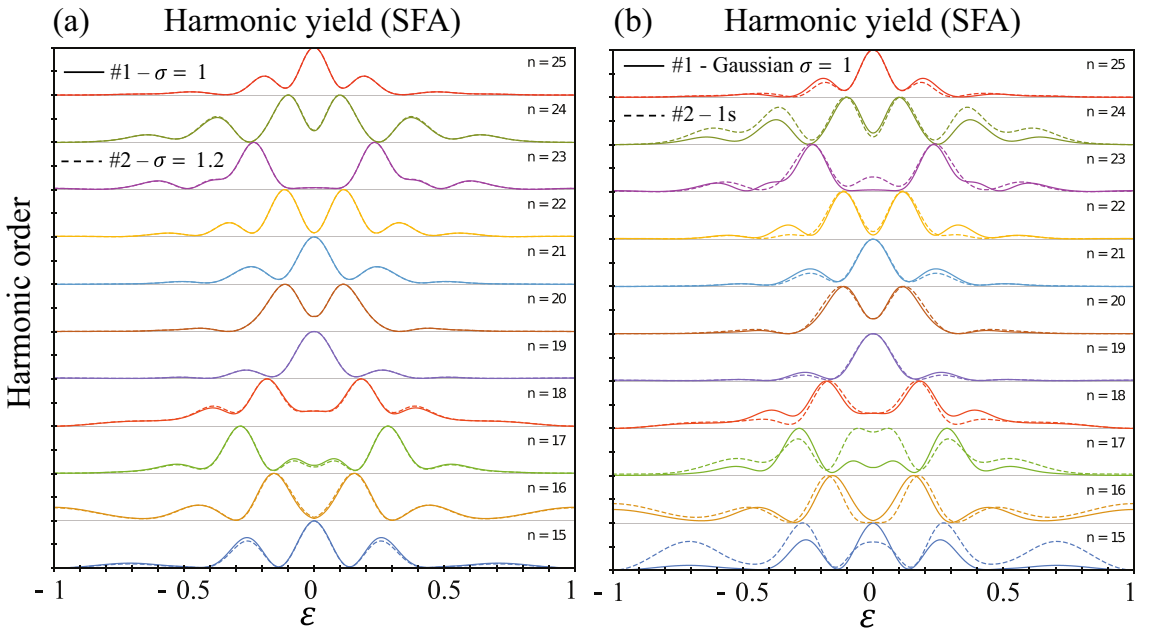

FIG. 7. Numerical results in model Ne using SFA: bi-elliptical (ω-2ω) HHG harmonic yield vs ε for $I_0 = 3 \times 10^{14}$ W/cm^2, $\Delta = 1/\sqrt{5}$, $\phi = \pi/2$, $\lambda = 800$ nm. The figure presents calculations in settings similar to those in Fig. 3(c) in the main text, but for (a) two Gaussian orbitals with sizes that vary by 20%. Notably, within the SFA there is no peak shifting between similar types of orbitals with different spatial extent, as observed with TDSE calculations. Also, the difference in harmonic yield between similar orbitals is substantially reduced compared to TDSE calculations. (b) A Gaussian orbital (full) compared to a hydrogen 1s orbital (dashed). Slightly stronger disparities are observed when the orbitals not only have different spatial extents, but also different shapes (Gaussian compared to exponential decay of 1s states).

APPENDIX E: SFA CALCULATIONS

In this Appendix we present numerical SFA results in the bi-elliptical HHG configuration for atomic species with an ionization potential set to that of neon, and using different valence orbital sizes. These results are comparable to those presented in the main text in Fig. 3 using TDSE calculations. We follow the technical approach in Refs. [20,67], and model orbitals of different spatial extents using Gaussian orbitals for which there are analytical expressions for the transition dipole matrix elements (with 20% difference in spatial extents). We also compare to results obtained using a hydrogenic 1s orbital. Results are presented in Fig. 7 with identical parameters to Fig. 3 in the main text.

Most features of the spectrogram obtained using TDSE calculations and experimentally are reproduced in the SFA calculations, including the dominant peak oscillation structure in the harmonics vs the ε axis, and the suppressed intensity of even harmonics at $\varepsilon = 0$. The exact relative intensities of the peaks, their positions along the ε axis, and the number of peaks differ for some harmonics between the TDSE and SFA results. Notably, there are much weaker disparities obtained for orbitals of different spatial extent, as compared to the TDSE [Fig. 7(a) compared to Fig. 3 in the main text]. This suggests that the SFA approach does not fully capture this phenomenon, though it is likely to describe it better if the level of approximations is reduced. Most importantly, we observe no effect of peak shifting between similar types of orbitals of

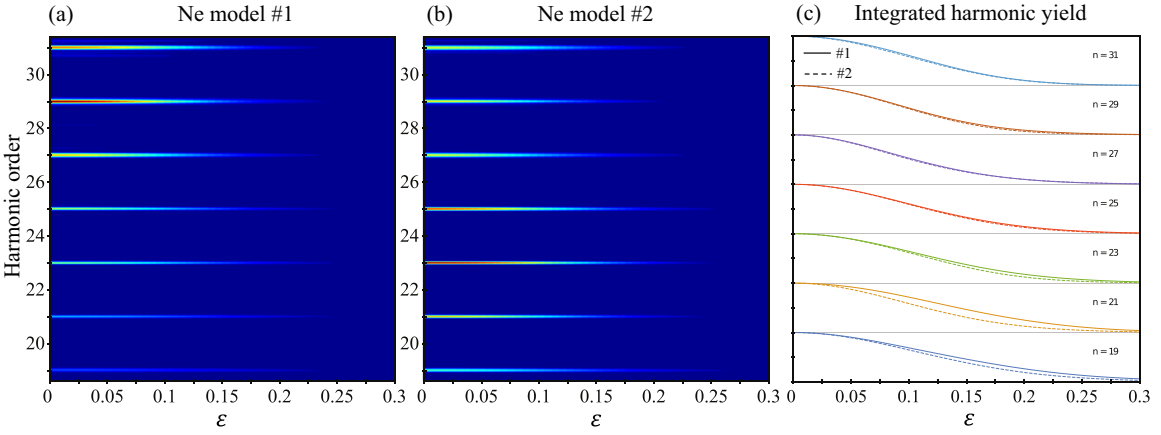

FIG. 8. Same as Fig. 3 in the main text, but for HHG driven by a monochromatic elliptical pump field with ellipticity ε.

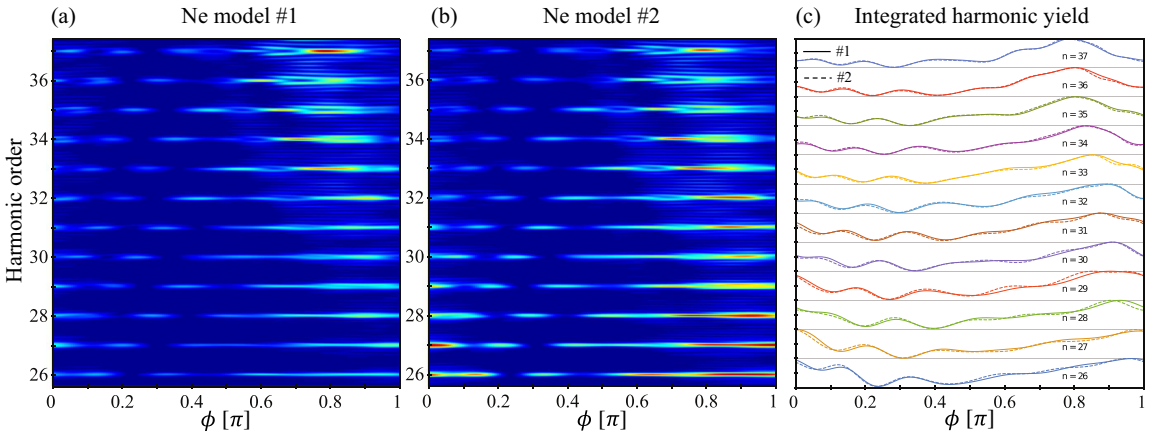

FIG. 9. Same as Fig. 3 in the main text, but for HHG driven by ω-2ω bi-chromatic colinearly polarized pumps with a relative phase ϕ.

different spatial extent in the SFA calculations, as expected, since Coulomb corrections are fully neglected in our SFA calculations. This result allows us to relate the peak shifting in the bi-elliptical spectrograms to the Coulomb corrections for electron trajectories in the continuum, which may be utilized for further spectroscopic purposes (e.g., of the dipole phase [56]).

We also note that slightly stronger disparities are observed in the SFA between different types of orbitals [hydrogenic 1s state compared to Gaussian; see Fig. 7(b)]. This is in agreement with TDSE calculations performed in He and Ne, suggesting that the bi-elliptical scheme is sensitive both to the orbital spatial extent, and to its shape (valence atomic shell type). Lastly, we note that the bi-elliptical HHG yield between different orbitals seems to reduce and vanish for higher-order harmonics in the SFA approach (though this is not observed in the TDSE calculations).

APPENDIX F: COMPARISON TO OTHER HHG SPECTROSCOPY METHODS

In this Appendix we present numerical results complementary to those presented in the main text in Fig. 3. We use the same EP models for Ne as in Fig. 3 in the main text, but replace the bi-elliptical HHG spectroscopy technique with two other standard HHG spectroscopy techniques for comparison: (i) Fig. 8 presents the HHG spectrogram from a monochromatic elliptical pump, where the pump ellipticity is scanned; (ii) Fig. 9 presents the HHG spectrogram from ω-2ω bi-chromatic pumps that are colinearly polarized, where the relative phase between the ω and 2ω beams is scanned. The driving fields used had the following form:

$$\vec{E}_{\rm elip}(t) = \frac{A(t)E_0}{\sqrt{1+\varepsilon^2}}{\rm Re}\{e^{i\omega t}(\hat{x}+i\varepsilon\hat{y})\},$$
$$\vec{E}_{\rm co-lin}(t) = A(t)E_0{\rm Re}\{e^{i\omega t}+\Delta e^{2i\omega t+\phi}\}\hat{x}, \quad \text{(F1)}$$

where all parameters are identical to those used in the bi-elliptical calculations. For monochromatic elliptical pumps, there is a slight disparity between the spectrograms of the two Ne models in the decay rates of the harmonic yield vs pump ellipticity. This effect is noticeable for harmonic 21, though for most harmonic orders the disparity is very small as compared to the disparities in Fig. 3 in the main text. For the colinearly polarized bi-chromatic pumps, there are some disparities in the spectrogram of both Ne models which are similar to those observed in the bi-elliptical spectrograms, e.g., peak broadening, peak minima and maxima shifting (for example in harmonic 28 near $\phi = 0.9\pi$). However, again, these effects are very small and almost non-noticeable. From this analysis, we conclude that the bi-elliptical HHG spectroscopy technique has enhanced sensitivity to the orbital spatial extent and atomic species as compared to other commonly used methods.

[1] T. Brabec and F. Krausz, Rev. Mod. Phys. **72**, 545 (2000).
[2] F. Krausz and M. Ivanov, Rev. Mod. Phys. **81**, 163 (2009).
[3] S. Ghimire, A. D. Dichiara, E. Sistrunk, P. Agostini, L. F. DiMauro, and D. A. Reis, Nat. Phys. **7**, 138 (2011).
[4] T. Schultz and M. Vrakking, *Attosecond and XUV Physics: Ultrafast Dynamics and Spectroscopy* (Wiley, New York, 2014).
[5] O. Kfir, S. Zayko, C. Nolte, M. Sivis, M. Möller, B. Hebler, S. S. P. K. Arekapudi, D. Steil, S. Schäfer, M. Albrecht, O. Cohen, S. Mathias, and C. Ropers, Sci. Adv. **3**, eaao4641 (2017).
[6] D. Shafir, H. Soifer, B. D. Bruner, M. Dagan, Y. Mairesse, S. Patchkovskii, M. Y. Ivanov, O. Smirnova, and N. Dudovich, Nature **485**, 343 (2012).
[7] O. Pedatzur, G. Orenstein, V. Serbinenko, H. Soifer, B. D. Bruner, A. J. Uzan, D. S. Brambila, A. G. Harvey, L. Torlina, F. Morales, O. Smirnova, and N. Dudovich, Nat. Phys. **11**, 815 (2015).
[8] E. Frumker, N. Kajumba, J. B. Bertrand, H. J. Wörner, C. T. Hebeisen, P. Hockett, M. Spanner, S. Patchkovskii, G. G. Paulus, D. M. Villeneuve, A. Naumov, and P. B. Corkum, Phys. Rev. Lett. **109**, 233904 (2012).
[9] P. M. Kraus, A. Rupenyan, and H. J. Wörner, Phys. Rev. Lett. **109**, 233903 (2012).
[10] O. Smirnova, Y. Mairesse, S. Patchkovskii, N. Dudovich, D. Villeneuve, P. Corkum, and M. Y. Ivanov, Nature **460**, 972 (2009).

[11] A. D. Shiner, B. E. Schmidt, C. Trallero-Herrero, H. J. Wörner, S. Patchkovskii, P. B. Corkum, J.-C. Kieffer, F. Légaré, and D. M. Villeneuve, Nat. Phys. **7**, 464 (2011).

[12] S. Pabst and R. Santra, Phys. Rev. Lett. **111**, 233005 (2013).

[13] J. Itatani, J. Levesque, D. Zeidler, H. Niikura, H. Pepin, J. C. Kieffer, P. B. Corkum, and D. M. Villeneuve, Nature **432**, 867 (2004).

[14] B. K. McFarland, J. P. Farrell, P. H. Bucksbaum, and M. Guhr, Science **322**, 1232 (2008).

[15] D. Shafir, Y. Mairesse, D. M. Villeneuve, P. B. Corkum, and N. Dudovich, Nat. Phys. **5**, 412 (2009).

[16] D. Bauer and K. K. Hansen, Phys. Rev. Lett. **120**, 177401 (2018).

[17] R. E. F. Silva, Á. Jiménez-Galán, B. Amorim, O. Smirnova, and M. Ivanov, Nat. Photon. (2019), doi:10.1038/s41566-019-0516-1.

[18] S. Long, W. Becker, and J. K. McIver, Phys. Rev. A **52**, 2262 (1995).

[19] A. Fleischer, O. Kfir, T. Diskin, P. Sidorenko, and O. Cohen, Nat. Photon. **8**, 543 (2014).

[20] E. Pisanty, S. Sukiasyan, and M. Ivanov, Phys. Rev. A **90**, 043829 (2014).

[21] O. Kfir, E. Bordo, G. Ilan Haham, O. Lahav, A. Fleischer, and O. Cohen, Appl. Phys. Lett. **108**, 211106 (2016).

[22] K. M. Dorney, L. Rego, N. J. Brooks, J. San Román, C.-T. Liao, J. L. Ellis, D. Zusin, C. Gentry, Q. L. Nguyen, J. M. Shaw, A. Picón, L. Plaja, H. C. Kapteyn, M. M. Murnane, and C. Hernández-García, Nat. Photon. **13**, 123 (2019).

[23] V. Averbukh, O. Alon, and N. Moiseyev, Phys. Rev. A **65**, 063402 (2002).

[24] D. Baykusheva, M. S. Ahsan, N. Lin, and H. J. Wörner, Phys. Rev. Lett. **116**, 123001 (2016).

[25] T. T. Luu and H. J. Wörner, Phys. Rev. A **98**, 041802 (2018).

[26] O. Smirnova, Y. Mairesse, and S. Patchkovskii, J. Phys. B **48**, 234005 (2015).

[27] D. Ayuso, P. Decleva, S. Patchkovskii, and O. Smirnova, J. Phys. B **51**, 06LT01 (2018).

[28] D. Ayuso, P. Decleva, S. Patchkovskii, and O. Smirnova, J. Phys. B **51**, 124002 (2018).

[29] Y. Harada, E. Haraguchi, K. Kaneshima, and T. Sekikawa, Phys. Rev. A **98**, 021401 (2018).

[30] D. Baykusheva and H. J. Wörner, Phys. Rev. X **8**, 031060 (2018).

[31] O. Neufeld, D. Ayuso, P. Declev, M. Y. Ivanov, O. Smirnova, and O. Cohen, Phys. Rev. X **9**, 031002 (2019).

[32] D. Ayuso, O. Neufeld, A. F. Ordonez, P. Decleva, G. Lerner, O. Cohen, M. Ivanov, and O. Smirnova, Nat. Photon. (2019), doi:10.1038/s41566-019-0531-2.

[33] S. Patchkovskii, Z. Zhao, T. Brabec, and D. M. Villeneuve, Phys. Rev. Lett. **97**, 123003 (2006).

[34] C. Vozzi, M. Negro, F. Calegari, G. Sansone, M. Nisoli, S. De Silvestri, and S. Stagira, Nat. Phys. **7**, 822 (2011).

[35] O. Neufeld and O. Cohen, Phys. Rev. Lett. **123**, 103202 (2019).

[36] L. Medišauskas, J. Wragg, H. Van Der Hart, and M. Y. Ivanov, Phys. Rev. Lett. **115**, 153001 (2015).

[37] E. Pisanty and Á. Jiménez-Galán, Phys. Rev. A **96**, 063401 (2017).

[38] L. Barreau, K. Veyrinas, V. Gruson, S. J. Weber, T. Auguste, J.-F. Hergott, F. Lepetit, B. Carré, J.-C. Houver, D. Dowek, and P. Salières, Nat. Commun. **9**, 4727 (2018).

[39] F. Ceccherini and D. Bauer, Phys. Rev. A **64**, 033423 (2001).

[40] V. Strelkov, Phys. Rev. Lett. **104**, 123901 (2010).

[41] O. Neufeld, E. Bordo, A. Fleischer, and O. Cohen, New J. Phys. **19**, 023051 (2017).

[42] O. Neufeld and O. Cohen, Phys. Rev. Lett. **120**, 133206 (2018).

[43] O. Neufeld, D. Podolsky, and O. Cohen, Nat. Commun. **10**, 405 (2019).

[44] O. E. Alon, V. Averbukh, and N. Moiseyev, Phys. Rev. Lett. **80**, 3743 (1998).

[45] O. Kfir, P. Grychtol, E. Turgut, R. Knut, D. Zusin, D. Popmintchev, T. Popmintchev, H. Nembach, J. M. Shaw, A. Fleischer, H. Kapteyn, M. Murnane, and O. Cohen, Nat. Photon. **9**, 99 (2015).

[46] C. Chen, Z. Tao, C. Hernández-García, P. Matyba, A. Carr, R. Knut, O. Kfir, D. Zusin, C. Gentry, P. Grychtol, O. Cohen, L. Plaja, A. Becker, A. Jaron-Becker, H. Kapteyn, and M. Murnane, Sci. Adv. **2**, e1501333 (2016).

[47] M. Kitzler and M. Lezius, Phys. Rev. Lett. **95**, 253001 (2005).

[48] C. M. Kim and C. H. Nam, J. Phys. B **39**, 3199 (2006).

[49] R. Cireasa, A. E. Boguslavskiy, B. Pons, M. C. H. Wong, D. Descamps, S. Petit, H. Ruf, N. Thiré, A. Ferré, J. Suarez, J. Higuet, B. E. Schmidt, A. F. Alharbi, F. Légaré, V. Blanchet, B. Fabre, S. Patchkovskii, O. Smirnova, Y. Mairesse, and V. R. Bhardwaj, Nat. Phys. **11**, 654 (2015).

[50] P. B. Corkum, Phys. Rev. Lett. **71**, 1994 (1993).

[51] J. Muth-Böhm, A. Becker, and F. H. M. Faisal, Phys. Rev. Lett. **85**, 2280 (2000).

[52] A. F. Alharbi, A. E. Boguslavskiy, N. Thiré, G. S. Thekkadath, S. Patchkovskii, B. E. Schmidt, F. Légaré, T. Brabec, V. R. Bhardwaj, and M. Spanner, Phys. Rev. A **96**, 043402 (2017).

[53] M. Y. Ivanov, T. Brabec, and N. Burnett, Phys. Rev. A **54**, 742 (1996).

[54] C. A. Mancuso, D. D. Hickstein, P. Grychtol, R. Knut, O. Kfir, X. M. Tong, F. Dollar, D. Zusin, M. Gopalakrishnan, C. Gentry, E. Turgut, J. L. Ellis, M. C. Chen, A. Fleischer, O. Cohen, H. C. Kapteyn, and M. M. Murnane, Phys. Rev. A **91**, 031402(R) (2015).

[55] K. Amini, J. Biegert, F. Calegari, A. Chacón, M. F. Ciappina, A. Dauphin, D. K. Efimov, C. F. de M. Faria, K. Giergiel, P. Gniewek, A. Landsman, M. Lesiuk, M. Mandrysz, A. S. Maxwell, R. Moszynski, L. Ortmann, J. A. Perez-Hernandez, A. Picon, E. Pisanty, J. S. Prauzner-Bechcicki *et al.*, Rep. Prog. Phys. **82**, 116001 (2019).

[56] D. Azoury, O. Kneller, S. Rozen, B. D. Bruner, A. Clergerie, Y. Mairesse, B. Fabre, B. Pons, N. Dudovich, and M. Krüger, Nat. Photon. **13**, 54 (2019).

[57] C. Cohen-Tannoudji, B. Diu, and F. Laloe, *Quantum Mechanics, Vol. 1*, 1st ed. (Wiley, New York, 1991).

[58] M. Abramowitz and I. A. Stegun, *Handbook of Mathematical Functions, with Formulas, Graphs, and Mathematical Tables* (National Bureau of Standards, U.S. Department of Commerce, Washington, DC, 1964).

[59] J. A. Fleck, J. R. Morris, and M. D. Feit, Appl. Phys. **10**, 129 (1976).

[60] M. D. Feit, J. A. Fleck, and A. Steiger, J. Comput. Phys. **47**, 412 (1982).

[61] K. Burnett, V. C. Reed, J. Cooper, and P. L. Knight, Phys. Rev. A **45**, 3347 (1992).

[62] M. A. L. Marques, A. Castro, G. F. Bertsch, and A. Rubio, Comput. Phys. Commun. **151**, 60 (2003).

[63] A. Castro, H. Appel, M. Oliveira, C. A. Rozzi, X. Andrade, F. Lorenzen, M. A. L. Marques, E. K. U. Gross, and A. Rubio, Phys. Status Solidi **243**, 2465 (2006).

[64] X. Andrade, D. Strubbe, U. De Giovannini, A. H. Larsen, M. J. T. Oliveira, J. Alberdi-Rodriguez, A. Varas, I. Theophilou, N. Helbig, M. J. Verstraete, L. Stella, F. Nogueira, A. Aspuru-Guzik, A. Castro, M. A. L. Marques, and A. Rubio, Phys. Chem. Chem. Phys. **17**, 31371 (2015).

[65] J. P. Perdew and A. Zunger, Phys. Rev. B **23**, 5048 (1981).

[66] C. Hartwigsen, S. Goedecker, and J. Hutter, Phys. Rev. B **58**, 3641 (1998).

[67] E. Pisanty, RB-SFA: Rotating bicircular high harmonic generation in the strong field approximation, https://github.com/episanty/rb-sfa, v1.0 (2014).